

Efficient PINNs: Multi-Head Unimodular Regularization of the Solutions Space

Pedro Tarancón-Álvarez^{1,2*}, Pablo Tejerina-Pérez^{1,2*},
Raul Jimenez^{2,3} and Pavlos Protopapas⁴

¹Departament de Física Quàntica i Astrofísica, Universitat de
Barcelona, Martí i Franquès 1, Barcelona, ES-08028, Barcelona, Spain.

²Institut de Ciències del Cosmos (ICC), Universitat de Barcelona, Martí
i Franquès 1, Barcelona, ES-08028, Barcelona, Spain.

³Institució Catalana de Recerca i Estudis Avançats, ICREA, Passeig
Lluís Companys 23, Barcelona, ES-08010, Barcelona, Spain.

⁴Institute for Applied Computational Science, Harvard University, 150
Western Ave., Allston, MA 02134, MA, USA.

*Corresponding author(s). E-mail(s): pedro.tarancon@fqa.ub.edu;
pablo.tejerina@icc.ub.edu;

Contributing authors: raul.jimenez@icc.ub.edu; pavlos@seas.harvard.edu;

Abstract

We present a machine learning framework to facilitate the solution of nonlinear multiscale differential equations and, especially, inverse problems using Physics-Informed Neural Networks (PINNs). This framework is based on what is called *multihead* (MH) training, which involves training the network to learn a general space of all solutions for a given set of equations with certain variability, rather than learning a specific solution of the system. This setup is used with a second novel technique that we call Unimodular Regularization (UR) of the latent space of solutions. We show that the *multihead* approach, combined with the regularization, significantly improves the efficiency of PINNs by facilitating the transfer learning process thereby enabling the finding of solutions for nonlinear, coupled, and multiscale differential equations.

Keywords: AI, PINNs, Transfer Learning, Multihead, Differential Geometry

1 Introduction

Non-linear differential equations describe complex systems in nature, such as fluid dynamics, climate modeling, and general relativity, to mention a few. While linear equations are widely applicable, non-linear equations often arise in systems where interactions or feedback loops create more intricate and unpredictable behaviors. Yet, in most cases, analytic solutions are either impossible or highly complex, necessitating the use of numerical methods to provide solutions [1]. With the advent of deep neural networks, particularly Physics-Informed Neural Networks (PINNs), it has become increasingly feasible to solve complex differential equations more efficiently. Extensive literature now exists on how to use PINNs to solve a wide variety of nonlinear, multiscale differential equations including those in complex, real-world systems where traditional numerical methods may struggle. An added layer of complexity arises when the goal is to solve inverse problems, where the objective is to infer unknown parameters or functions within a system based on available data, such as initial or boundary conditions [2].

Here, we present two efficient algorithms to use in PINNs that are aimed at significantly improving the solution of inverse problems for non-linear, coupled and multi-scale differential equations (DEs). The first technique is called *multi-head* training, where we train the network to learn the general space of all solutions (or latent space) to different variations of the same DEs, from which we can perform transfer learning to different regimes [3–8]. The second one is a novel technique that we call *uni-modular regularization* of the latent space of solutions. It is based on the computation of the metric tensor, a concept from differential geometry, induced on the latent-space-hypersurface. This second technique facilitates (or even unlocks) the transfer learning process to extreme regimes by ensuring a more controlled response of the latent space to changes in the DEs [9].

There are previous works where concepts of differential geometry have been used in the context of NNs. In [10] the authors explore and characterize the behavior of NNs during training through the theory of Riemannian geometry and curvature - they relate the output of the NN with the input transformations through the curvature equations. An analysis and comparison between the convergence properties of the metric of NNs (used for classification) and the metric under the Ricci-DeTurck flow is done in [11]. In [12, 13], the authors remove edges of low importance (prune) the computational graph using the definition of Ricci curvature. To the best of our knowledge, differential geometry techniques have not been used in order to increase the performance of PINNs.

Using PINNs to solve DEs offers several advantages over traditional methods. For instance, a PINN can be trained on a specific range of boundary conditions (BCs) or initial conditions (ICs). The specific solution(s) to a DE can only be determined if the corresponding ICs or BCs are specified as part of the problem. The existence and uniqueness theorem [14] ensures that there is a unique solution for a set of DEs once specific ICs or BCs are chosen. In traditional numerical methods, numerical integration is performed for each set of initial and boundary value conditions (IC-BV). If multiple IC-BVs are given, the numerical integration must be run separately for each one. However, for PINNs, we can train the NN on a specific set of DEs in a given range of IC-BVs referred to as a *bundle*, which must be sampled [15]. The training process may

take more computational resources. However, once trained, the PINN can be evaluated almost instantaneously [16, 17] for any choice of IC-BV within the bundle, even if it was not trained specifically on it, and will still yield a solution. This may be extremely useful in cases where a very large number of solutions is required, each corresponding to different initial and boundary value conditions (IC-BV) or parameters [18].

Stiff DEs, e.g. DEs where there is a large separation of scales between different features of the solution, can be challenging to solve [19]. Stiffness can manifest in various forms, including eigenvalue-based stiffness (where the system’s Jacobian has widely varying eigenvalues), multi-scale stiffness (involving both fast and slow time scales such as the flame equation¹ in Sec. 3.1), damping-induced stiffness (common in physical systems with strong damping such as the Van der Pol equation Sec 3.2), non-linear stiffness, interval-dependent stiffness, and transient stiffness [20]. In the cases we present, traditional numerical methods are capable of solving the equations. However, in the context of solving DE systems with PINNs, we present novel techniques that significantly improve, or even unlock, our ability to solve them [21]. Moreover, these techniques are particularly relevant when there is no established numerical setup to solve the problem. This is the case of inverse problems. PINNs are a well-suited tool for solving such problems [17], as we will explain through the example of Sec. 3.3 (for a thorough analysis of this example see [22]).

The purpose of this article is to introduce these techniques and show their efficiency with several examples. The algorithms that we present here are of general use in solving differential equations and inverse problems. The article is structured as follows: in section 2 we introduce the methodology used; we describe the NN structure in 2.1 and 2.2, the general training procedure in 2.3, and unimodular regularization in 2.4. The application of these techniques to different ODE systems and results are presented in section 3; we solve the Flame Equation in 3.1, the Van der Pol Oscillator in 3.2, and Einstein Field Equations in 5-dimensional Anti de Sitter spacetime in 3.3. The conclusions are summarized in section 4.

2 Methodology

Physics-Informed Neural Networks (PINNs), first introduced in the works of Disanayake and Phan-Thien [23] and Lagaris et al. [24], have emerged as a powerful framework for solving partial and ordinary differential equations (PDEs/ODEs). Raissi et al. [21] popularized this approach by demonstrating its effectiveness on a variety of challenging physical problems, while other researchers have made significant advancements in applying neural networks to PDEs and ODEs, including notable examples such as [25–27]. In this paradigm, one typically trains a distinct neural network for each unknown function in the governing equations. The training process involves minimizing a loss function that encodes the squared residuals of these differential equations, thereby embedding the physics directly into the learning objective.

While traditional numerical methods often outperform PINNs in terms of computational efficiency and accuracy, PINNs offer unique advantages. One key benefit

¹Strictly speaking, the flame equation exhibits multiple types of stiffness.

is their ability to learn the parametric dependence of solutions with respect to varying equation forms or initial/boundary conditions (IC/BC). In contrast, traditional methods typically require rerunning the solver for each set of different IC/BC. With PINNs, however, it is possible to train the network to simultaneously accommodate multiple conditions, enabling rapid evaluation of solutions for various IC/BC values or even different, parametrically related equations. This allows us to attack otherwise untreatable problems, like recovering a free form function appearing on the equations from different initial/boundary data of the unknown functions. Another notable advantage of using PINNs is their ability to leverage transfer learning, as discussed in Sec. 2.3. Transfer learning allows the model to generalize beyond the range of its training data, enabling the prediction of solutions in unseen regions or conditions. This technique has proven crucial for obtaining solutions in the stiffer regimes of certain differential equations [8]. Throughout this paper, we will leverage this concept within the so-called Multi-Head (MH) framework.

The MH approach to solve DEs with PINNs aims to train a model that learns a general solution space for a given system, accommodating variations such as different ICs, BCs, coefficients/parameters, or forcing functions f in the inhomogeneous part of the DE problem. Rather than learning a single specific solution, the model learns how the solution space behaves under all these different factors, allowing for generalization across a range of possible scenarios.

To formalize this approach, we represent the DE system as follows:

$$\mathcal{D}\psi(x^\mu) - f(x^\mu) = 0 \quad ; \quad \mu = 1, 2, 3 \dots \quad (1)$$

where each x^μ represents a vectorial quantity of dimension equals to the batch size. \mathcal{D} is a generic differential operator that encodes the form of the DE system, x^1 is the independent variable, $x^{2,3,\dots}$ a list of parameters describing the solutions for different ICs, BCs or parameters of the equations, and $\psi(x^\mu)$ is the solution of the system. $f(x^\mu)$ is a general function (often called the inhomogeneous part) that depends on the independent variable and could admit also a parameter.

From this point forward, we will refer to any scenario with the same DE form (same \mathcal{D}) and some choice of ICs, BCs, parameters ($x^{2,3,\dots}$) and/or forcing functions f as belonging to the same *family* of DEs. Any variation of $x^{2,3,\dots}$ and/or f will be a variation within the family of the DEs, and a specific choice of them will be an *element* of the family of DEs.

The multi-head (MH) approach is based on learning a mapping to a higher-dimensional latent space that goes beyond the specific solutions of the differential equations. In this higher-dimensional space, all potential solutions are encoded for variations within the family of DEs. In the context of PINNs, this latent space is represented by a set of d functions, $H_i(x^\mu)$, which are generated by the *body* neural network (NN), whose output dimension is d .

The latent space of solutions can then be “projected down” to a specific solution for a given element of the family of the DE system by non-linearly combining the d components. This projection is performed by another NN, known as the *head*. We will describe the multi-head setup in detail in the following sections. For pedagogical clarity, we will first discuss a single-head model to explain its implementation within

the PINNs framework. Subsequent subsections will show how this approach can be generalized to multiple *heads* and how the latent space can be learned to extrapolate solutions to regions where the body has not been trained—a process known as transfer learning. Finally, we will introduce a novel technique called *Unimodular Regularization*, which improves the performance of the MH approach when transferring solutions to stiff regimes of differential equations.

2.1 Single-head

The *single-head* approach involves using the latent space components $H_i(x^\mu)$ and passing them through a linear layer or another NN that produces the desired output dimension for the specific solution (in the case of a simple ODE, this would be a scalar output, i.e., the solution to the system). The structure responsible for processing $H_i(x^\mu)$ is called a *head*, which projects the latent space into the specific solution:

$$\psi(x^\mu) = \text{head}_W [H_i(x^\mu)] \quad (2)$$

where W represents the weights and biases of the *head*, as shown in Fig. 1

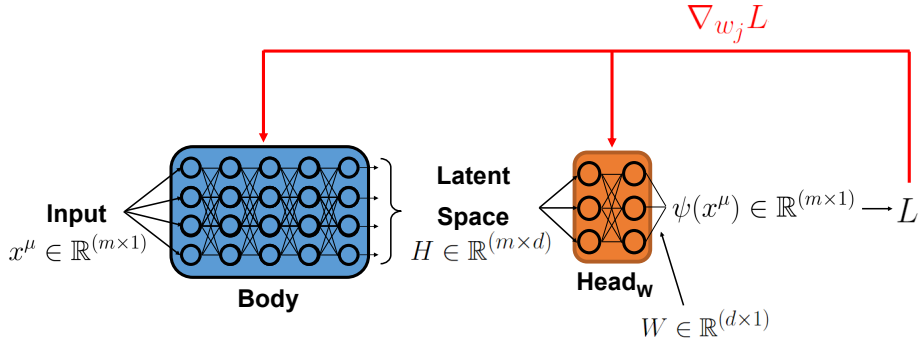


Fig. 1 Scheme of the single head approach - we can see how this simplified case is the standard case for a deep neural network with multiple hidden layers and one single output. The output solutions are calculated as $\psi^{\text{NN}} = \text{head}_W (H)$ with $\psi \in \mathbb{R}^{(m \times 1)}$, $H \in \mathbb{R}^{(m \times d)}$ and $W \in \mathbb{R}^{(d \times 1)}$, being m the batch size (number of points sampled in the independent variable x^1 meshed with sampling of $x^{2,3,\dots}$), and d the number of neurons in the last layer of the head. The loss L is of the form in Eq. (3). The red arrow represents the updating of the NN-parameters w_j (weights and biases) based on minimization of the loss function through gradient descent (represented by $\nabla_{w_j} L$).

In this simple case with a single head, we essentially have the standard setup of a NN with one output as the solution to an ODE problem. The parameters of the head and the body are initialized randomly and optimized by minimizing the loss using the Adam optimizer. The loss function consists of the squared residuals of all DEs, averaged over the number of equations, sampled points along the independent variable, different ICs/BCs, parameters, and forcing functions. We can express the loss function for our PINN as follows:

$$L_{\text{DE}} = \sum_{\mu=1}^n \sum_{\text{eqs}} [\mathcal{D}\psi^{\text{NN}}(x^\mu) - f(x^\mu)]^2 \quad (3)$$

where ψ^{NN} is the solution predicted by the NN, and is guaranteed to satisfy the IC/BC by construction (see ref. [8, 24] for details).

The sum over μ represents the total over the different elements of the DE system, including also all sampled points along the independent variable x^0 . Finally, the sum² over the equations is the total of the residuals for each equation in our system of DEs.

2.2 Multi-head

We are now ready to understand how multiple heads enable the NN to learn the latent space of solutions across a whole family of DEs.

The goal is to find a specific solution $\psi_\alpha^{\text{NN}}(x^\mu)$ for each problem by projecting H into a reduced space, non-linearly combining its components through a head with parameters W_α , where the index α labels different variations of the DE family. Each head W_α correspond to a specific DE variation and produces a loss L_α as described in Eq. 3. We then define the total loss at each iteration as follows:

$$L_{\text{tot}} = \sum_{\alpha=1}^{\#\text{heads}} L_\alpha \quad (4)$$

and we perform gradient descent on the total loss. Thus, the MH PINN simultaneously solves all specified DE problems.

This approach uses one NN for each problem, with the *body* shared across all NNs. Thus, the *body* captures the global properties of the solutions, ideally representing the entire family of equations.

²Note that the distinction between summing and computing the mean is irrelevant, as it merely scales the loss by a factor inversely proportional to the number of sampled points.

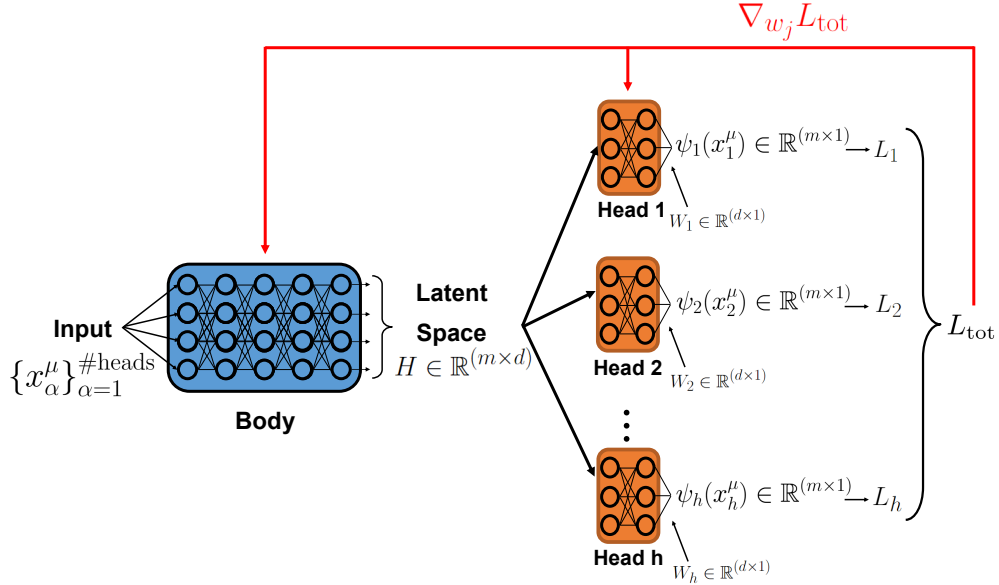


Fig. 2 Scheme of the multi-head approach. The index α in the inputs x_α^μ denotes all the variations within the DE family - all of them are inputs to the *body*, but each specific element of the family is later solved by its corresponding *head*, giving solutions $\psi_\alpha(x_\alpha^\mu)$ as output ($\alpha = 1, \dots, h$). The total loss L_{tot} is as defined in (4). The backpropagation of the derivatives $\nabla_{w_j} L_{\text{tot}}$ indicated by the red arrow updates all the weights and biases w_j (both of the *body* and all *heads*).

2.3 Training and transferring

The *body* H is trained using standard gradient descent techniques, with the loss function defined in Eqs. (3) and (4). As shown in the previous section and in Fig. 2, each *head* specializes in a specific variation within the family of DEs. If we continue training the *body* and *heads* with sufficiently diverse set DE elements, we expect the latent space H to converge to a stable set of function values as the loss flattens.

Once the latent space H stabilizes, we freeze the parameters of the *body*³, so they no longer change, even as the model continues training. We denote the frozen *body* as H^f .

The pre-training of the latent space H can be applied to solve any new variations of the DE family by simply attaching a new *head* that takes H^f as input. This process is referred as transfer learning (TL). The only part that requires training is the set of parameters \widetilde{W} for the new *head*, which is much smaller and computationally less expensive (see Fig. 3):

$$\psi_{\text{new}}^{\text{NN}} = \text{head}_{\widetilde{W}}(H^f). \quad (5)$$

³Freezing the parameters of the *body* implies detaching the tensors of H .

The process of transfer learning (TL) can be used to interpolate, i.e. to obtain solutions for new elements of the DE family given by choices of parameters/IC/BC/-forcing functions whose values fall within the range of training of the *body* H^f . TL can also be used for extrapolation; it can be used to find a specific solution to a variation within the DE family, even if that variation lies outside the values used in training. This is often the case when transferring to stiffer regimes. Next, we present a new technique used during training and show that it improves results during the transfer learning phase.

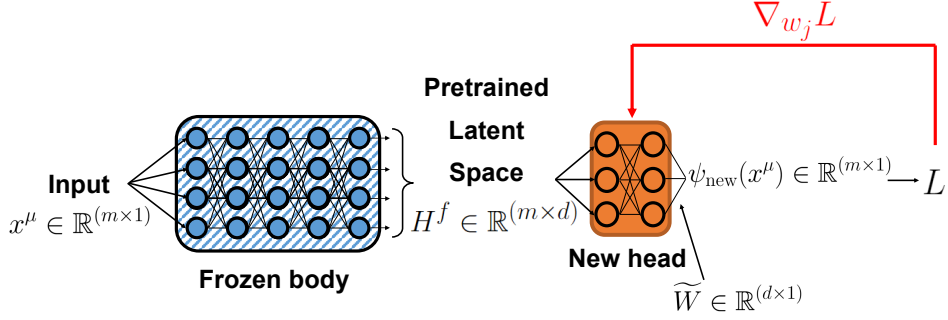


Fig. 3 Scheme of the transfer learning procedure from a pre-trained *body* through the MH approach of section 2.2. The blue, diagonal lines in the *body* indicate that it is frozen, i.e. its weights and biases do not change. Only the weights of the new *head* are learnt in order to find the solution to a new variation of the DE system, as indicated by the red arrow. As explained in the text, this method can be used both for interpolation and extrapolation of solutions from the pretrained latent space.

2.4 Unimodular regularization

In this subsection, we introduce Unimodular Regularization (UR), a novel technique developed as part of the MH setup. This method involves imposing specific constraints on the values of the latent space and its derivatives, enabling the MH framework to generalize effectively across variations within the family of DEs. By regularizing the latent space in this manner, we enhance its adaptability and ensure robust transfer learning capabilities. The method’s theoretical foundations and technical implementation are detailed below.

As we have previously discussed, the *body* NN in a MH setup is a critical component. Its primary function is to learn a generalized latent space of solutions, which serves as a functional basis for the problem. This latent space captures the underlying structure of the solution space of a family of DEs, and enables the model to represent a wide range of behaviors. The *head* of the network then nonlinearly combines this latent space for a specific element of the DEs family to produce the corresponding solution. This separation between the generalized latent representation (*body*) and specific parametrization (*head*) ensures both flexibility and efficiency in solving the DEs. We denote the latent space functions as H_i , where i ranges from 1 to d , with

d representing the dimension of the latent space. This latent space is determined by the inputs provided to the model, which we denote by x^μ . Here, μ ranges from 1 to n , where n is the number of inputs of our model.

Amongst these inputs, x^1 will always be the independent variable of the DE. The remaining variables, x^2, x^3, \dots, x^n , belong to parameter space and characterize different elements of the same family of DEs, and thus different solutions. These include variations due to different IC or BC, or specific parameter values or forcing functions within the DE itself. The exact nature of this parameter space depends on the problem being addressed.

During the training process, the *body* of the MH will learn a latent space $H_i(x^\mu)$ that generalizes common features across different solutions to the DE within the same family. However, the choice of this set of functions is not unique, as the DEs are not *exactly* solved during training⁴, and the *heads* simultaneously learn how to combine these functions to produce specific solutions non-linearly. This introduces a potential problem: some learned latent spaces may not generalize well to regions of the parameter space outside the training range. Specifically, if the latent space exhibits rapid variation with respect to the input parameters x^μ , TL to new parameter ranges may become problematic. In such cases, the frozen latent space may take significantly different values for variations within the family of DEs that are close to each other. This often happens when the equations are stiffer in these ranges⁵. The *head*, in turn, would need to produce arbitrarily large responses to compensate for these rapid variations, making the solution unreliable.

To address this issue, we have developed a novel method called Unimodular Regularization (UR). This approach quantifies the values of the latent space and its derivatives by computing the associated metric tensor. By constraining the behavior of the latent space in this way, we ensure improved generalization and stability during TL, particularly in regions where the equations are more challenging. This is inspired by an alternative theory to General Relativity called Unimodular Gravity. In this theory the determinant of the metric tensor is picked to be -1 and the Gauge Group is reduced from diffeomorphisms (General Coordinate Transformations) to Transverse Diffeomorphisms (TDiff). These transformations are the ones that leave the determinant of the metric invariant. For more details see [28, 29].

We begin by embedding the latent space into the input space. This is achieved by parametrizing the latent space as a hyper-surface using the inputs x^μ . To formalize this, we group all components into the following vectorial quantity

$$\vec{\Omega} = (x^\mu, H_i(x^\mu)) \quad (6)$$

where the total dimension of $\vec{\Omega}$ is given by $M = d + n$. Using standard techniques from differential geometry, we can compute the induced metric tensor on the hyper-surface

⁴The DEs are solved by PINNs to the accuracy given by the square root of the loss function at a certain stage along the training.

⁵This is typically the case in MH techniques, which are often used for TL in parameter ranges where the DEs are stiffer.

with the following expression:

$$g_{\mu\nu} = \frac{\partial \vec{\Omega}}{\partial x^\mu} \cdot \frac{\partial \vec{\Omega}}{\partial x^\nu}. \quad (7)$$

Here, \cdot denotes the usual scalar product⁶. It is important to note that $g_{\mu\nu}$ is a matrix of dimension $n \times n$. Notably, as the metric tensor $g_{\mu\nu}$ is computed according to (7), some entries of this matrix will be proportional to the derivatives of the latent space with respect to its inputs. These entries, therefore, quantify the sensitivity of $H_i(x^\mu)$ to the inputs.

To extract a scalar quantity from $g_{\mu\nu}$ that retains this sensitivity information we define the quantity g as

$$g = \det g_{\mu\nu} \quad (8)$$

where \det represents the determinant of the metric tensor. Note that, by definition, this quantity is always greater than or equal to 1.

Up to this point, we have introduced a method to use a scalar quantity, g , to quantify the sensitivity of the latent space to the model’s inputs. Since our goal is to ensure this response is as smooth as possible, we now turn on how this can be imposed during the model’s training process. In the PINNs setup, the first step is to select a sampling of points for the independent variable and the parameters of the DE. The total number of points chosen is referred as the batch size. These inputs, denoted by x^μ , constitute our training set. Once the sampling points are fixed, the response of the latent space $H_i(x^\mu)$ can be trivially evaluated at these points.

The implementation of expression (7) is straightforward, as the required derivatives can be computed analytically through automatic differentiation. This results in an $n \times n$ matrix for each point in the batch, yielding a total size = batch size $\times n \times n$. To simplify this structure, we use expression (8) to compute a scalar quantity for each point in the batch, reducing the dimensions to match the batch size. This scalar function quantifies the sensitivity, or rate of change, of the latent space with respect to the chosen input points.

To ensure that this rate of change remains smooth, we introduce an additional term to the loss function, denoted as L_{UR} , which takes the following form:

$$L_{UR} = \lambda \sum_{\text{batch}} \left[\sqrt{g(x^\mu)} - \vec{\mathcal{I}} \right]^2. \quad (9)$$

Here, $\vec{\mathcal{I}}$ is a vector of ones with a length equal to the batch size, and λ is a free parameter that quantifies the relative weight of this term with respect to the differential equation loss. It is crucial to select λ appropriately; if it is too large, the latent space response will become nearly constant, preventing the *head* from projecting it to the desired solution. In our experiments, λ was chosen to lie between 10^{-7} and $5 \cdot 10^{-5}$, depending on the specific equations under consideration.

⁶The scalar product used here is defined as $\vec{x} \cdot \vec{y} = x_1 y_1 + x_2 y_2 + \dots + x_n y_n$ where the dimension of each of the vectors is n .

The choice of using \sqrt{g} is motivated by General Relativity. However, we expect to obtain similar results using g instead of \sqrt{g} . Also note that because of the definition of the metric tensor, its determinant is always positive.

Since computing g is computationally intensive, we only considered this additional loss every N epochs. For epochs that are not divisible by N , the term is set to zero. Finally, if the model involves multiple bodies (as is often the case when the DE system includes more than one unknown function), the metric must be computed separately for each body. Consequently, for every unknown function in the system, a corresponding term of the form (9) is added to the total loss.

3 Results

In this section, we apply the proposed methods to three different ODEs of increasing complexity. First, we address the flame equation, a first-order, non-linear ODE that presents a challenge due to its rapid growth for specific initial conditions. Next, we tackle the van der Pol oscillator, a second-order, non-linear ODE that is reformulated as a system of two first-order ODEs. Finally, we will apply the method to an inverse problem: recovering a free function and solving a system of coupled, first-order, non-linear ODEs with different BC for the unknown functions. This problem, motivated by holography, involves solving the Einstein Field Equations (EFE) with a scalar field.

We demonstrate that the proposed method successfully handles all three problems. Moreover, by imposing UR during the training of the body, the solutions obtained can be effectively transferred to more challenging regimes.

The structure of the following subsections will be consistent across the cases discussed. First, we train the *body* of the MH setup using different *heads*, each projecting the latent space toward the desired solutions for specific values of a given parameter or IC/BC (specific realizations of an element within the same family of ODEs). This training process will be performed twice: once with UR and once without it. Notably, the solutions obtained during this initial training phase appear identical in both cases.

Next, we will conduct TL by freezing the parameters of the *body* and training a new *head* for values of the parameter/IC/BC where the solutions are stiffer. In some cases, a proper solution through TL is only achievable when using a modified latent space geometry, which we refer to as the “regularized metric”. To highlight this, we will compare the performance of the standard MH setup (no UR) with the modified “UR MH” setup. This comparison shows that, under conditions of extreme stiffness, the MH with UR setup facilitates TL much more effectively—or even exclusively—when the standard MH approach fails to converge to a solution. By incorporating UR, we further enhance the stability and generalization of the MH approach.

The results shown in this section were obtained by training the models on a single NVIDIA A30 graphic card. The total process of training the body and then learning a new head to transfer learn took few days in the most computationally demanding case (EFE).

3.1 Flame equation

The flame equation describes the growth of a flame ball with radius y as a function of the time t , starting from a fixed initial value δ . The amount of consumed oxygen during combustion inside the ball scales with the volume $\sim y^3$ and the flux of incoming oxygen scales with the surface area $\sim y^2$. Different values of δ imply different realizations of the ODE as an element within the family of flame equations. This equation and the proper IC can be written in the following form

$$\frac{dy}{dt} = \rho(y^2 - y^3); \quad y(0) = \delta : \quad 0 \leq t \leq \frac{2}{\delta\rho}. \quad (10)$$

where we have introduced an additional parameter ρ that will artificially increase the stiffness of the problem. In our case we are choosing ρ to be 300. As we have mentioned, the solution to this equation will present a rapid growth on a time scale $2/\delta\rho$. This growth will be faster as we decrease δ . Thus, the problem will be stiffer for smaller values of δ .

The strategy for applying our method is as follows. We will first train two different *bodies* using four *heads* for $\delta \in [0.02, 0.04]$, for $1.5 \cdot 10^6$ epochs. In one of them, we will impose UR as an additional loss. The results obtained for the solutions and the determinant of the metric are shown in figure 4.

Next, we will freeze the *body* in both cases and perform TL by training a new head from scratch for a value of $\delta = 0.015$. The results of this TL are shown in figure 5, along with the relative error between the numerical and the NN solutions, computed as

$$RE[\%] = \frac{|y^{\text{RK4}}(t) - y^{\text{NN}}(t)|}{1 + |y^{\text{RK4}}(t)|} \cdot 100 \quad (11)$$

where we have added the +1 factor in the denominator to avoid dividing by zero.

The model architecture and training details are summarized here. The *body* is a Fully-Connected Neural Network (FCNN) with two input units, 64 output units, and three layers of 64 neurons each. Each *head* is an FCNN with 64 input units, one output, and two layers of 32 neurons each, using `Tanh` as the activation function. For MH *body* training, we used `adam` as the optimizer with an initial learning rate of $1 \cdot 10^{-3}$, reduced by 5 every 15,000 epochs using a step scheduler. TL followed the same parameters for both bodies but used a higher learning rate ($5 \cdot 10^{-3}$), reduced by 2.5% every 2,500 epochs.

For training, we sampled 100 points in the t -direction between the time bounds in (10), adding small random noise at each epoch to prevent overfitting. When training the MH *body*, we used $\delta = 0.02$ (the smallest value in the range) to ensure the widest time intervals. For UR, we set $\lambda = 5 \cdot 10^{-7}$ and imposed the additional loss term every 100 epochs.

3.2 Van der Pol oscillator

The van der Pol oscillator represents a specific instance of a non-linear, damped harmonic oscillator. It can be mathematically characterized by the subsequent

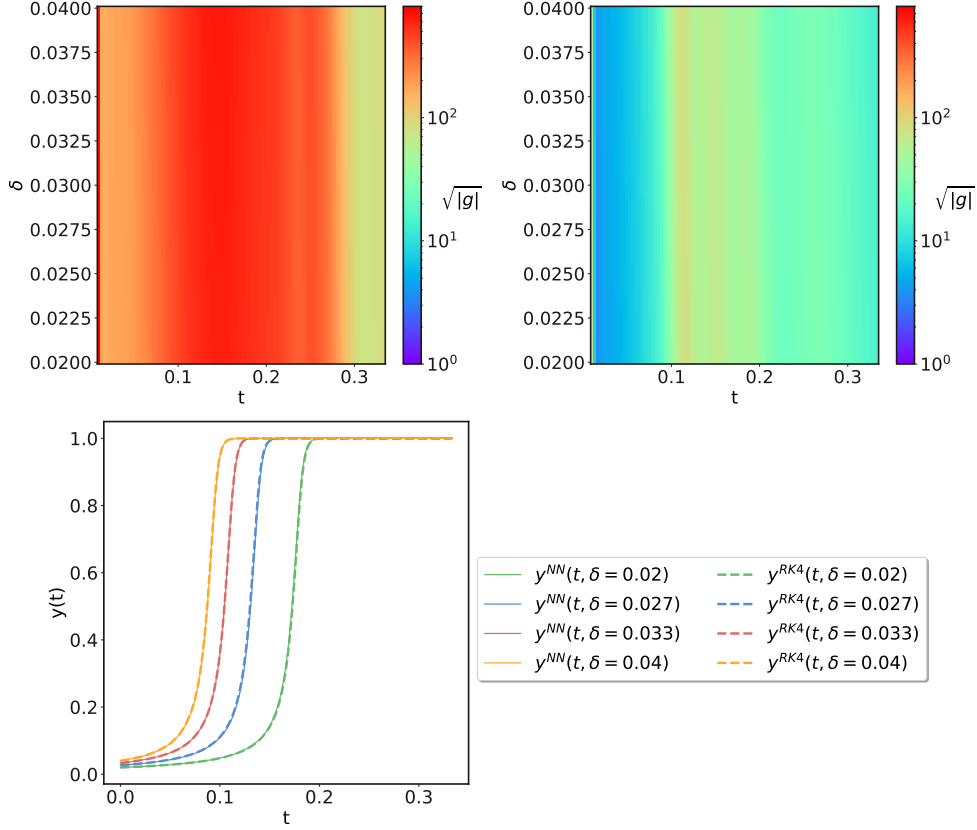


Fig. 4 Training of the MH *body* for the flame equation. **Top:** Metric determinant without UR (left) and with UR (right). Note the difference in one to two orders of magnitude for the values of g in each case. **Bottom:** Solutions to the flame equation $y^{NN}(t)$ (solid lines) compared with the numerical-RK4 solutions (dashed lines) for each of the *heads*, for values of the parameter $\delta \in [0.02, 0.04]$. As noted in the text, these solutions look identical for both cases with and without UR in the MH training process.

second-order ODE along with the IC:

$$\frac{d^2 x}{dt^2} - a(1 - x^2) \frac{dx}{dt} + x = 0; \quad x(0) = 1; \quad \left. \frac{dx}{dt} \right|_{t=0} = 0, \quad (12)$$

where $x(t)$ can be understood as the oscillator's position over time. In this context, a is regarded as a damping coefficient and modulates the problem's stiffness. The greater its value, the more challenging the equation will be to resolve. A key distinction between this equation and the preceding case is that it represents a second order ODE. Therefore, for the PINNs method to efficiently converge to the desired solution, it is advantageous to transform equation (12) and the IC into a system of two first order

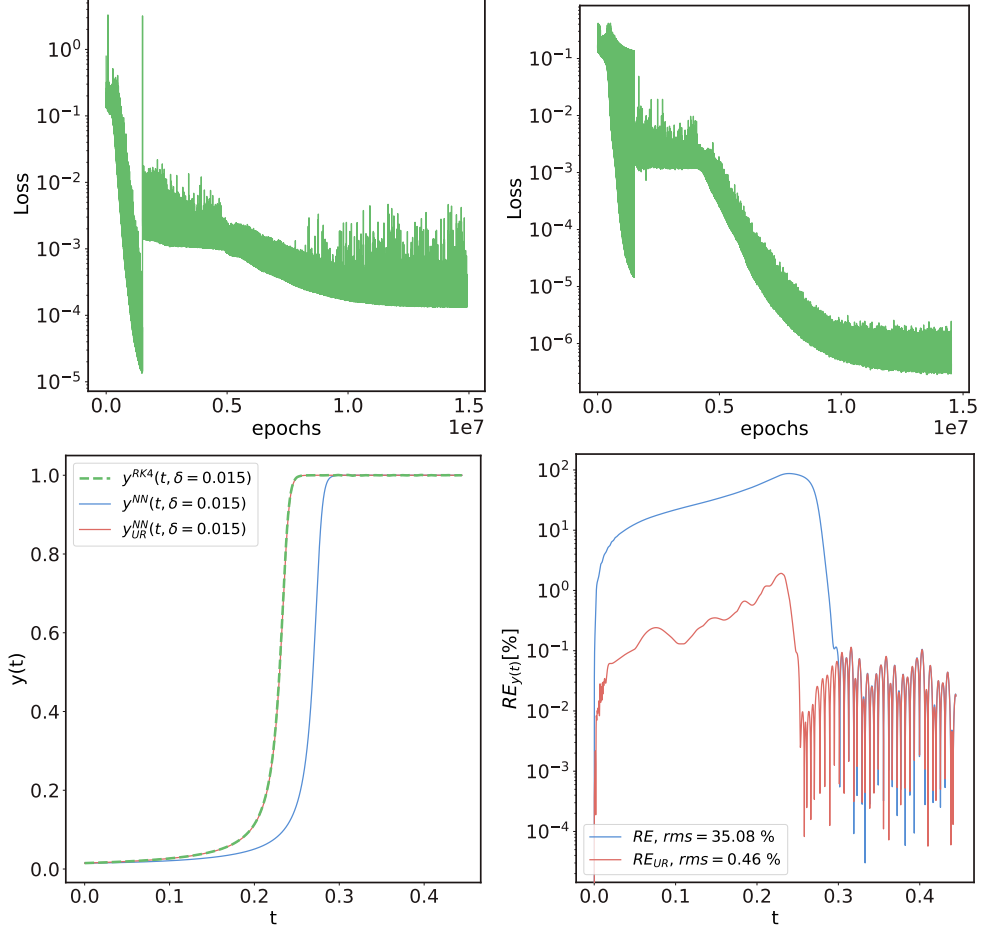


Fig. 5 TL for the flame equation for $\delta = 0.015$. **Top:** Loss functions for cases without UR (left) and with UR (right). TL starts at epoch $1.5 \cdot 10^6$. **Bottom left:** Solutions for $y(t)$ from a *body* with UR (solid red line), without UR (solid blue), compared to the numerical solution (dashed green). **Bottom right:** Relative error (in %) for cases with UR (red) and without UR (blue), as defined in Eq. (11). In the legend, we show the value of the root mean square (rms) for each case.

ODEs by introducing an auxiliary unknown function $y(t)$.

$$\begin{cases} \frac{dx}{dt} = \rho y \\ \frac{dy}{dt} = \rho a(1 - x^2) + \rho x \end{cases} \quad \text{IC: } \begin{cases} x(0) = 1 \\ y(0) = 0. \end{cases} \quad (13)$$

As in the previous case, we have additionally introduced ρ as a parameter to artificially increase the stiffness of the problem in the domain of interest. Throughout this subsection, we will fix it at 10.

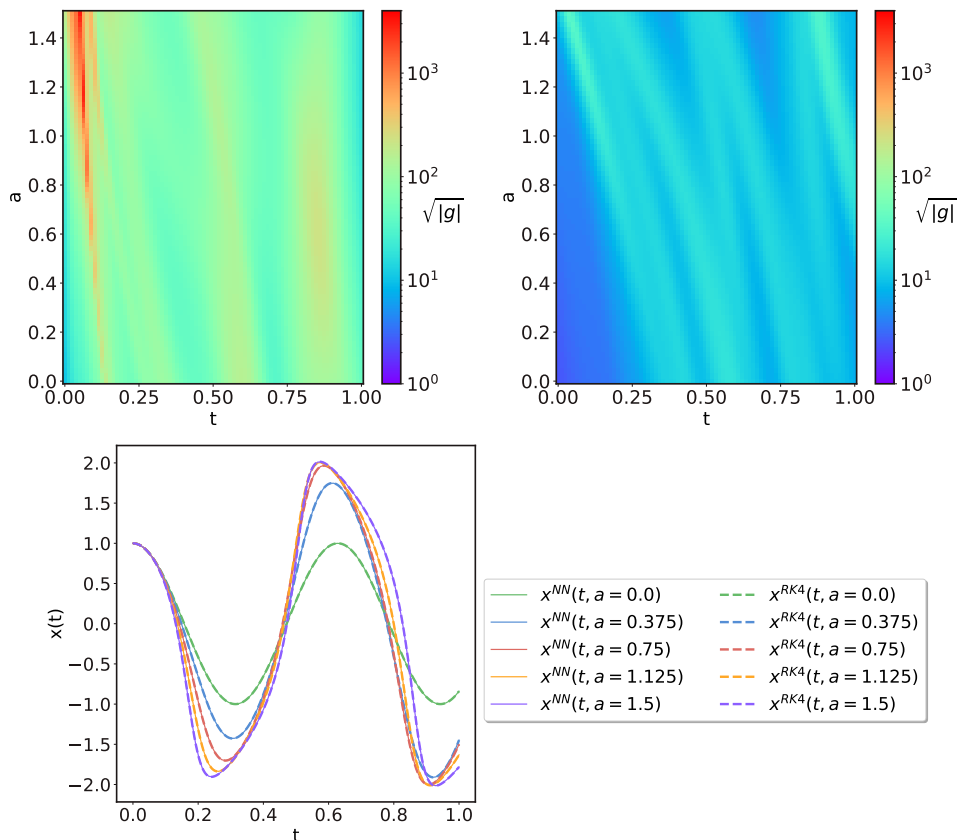


Fig. 6 Training of the MH *body* for the van der Pol oscillator. **Top:** Metric determinant of the $y(t)$ *body* without UR (left) and with UR (right). **Bottom:** Solutions to the van der Pol oscillator $x^{NN}(t)$ (solid lines) compared with the numerical-RK4 solutions (dashed lines) for each of the *heads*, for values of the parameter $a \in [0.0, 1.5]$. The solutions look identical for both cases with and without UR in the MH training process.

The primary distinction between this case and the previous one lies in our treatment of x and y as independent functions. Consequently, we introduce an additional NN to serve as the extra function. The MH strategy will largely remain unchanged, except for the necessity of training one more NN. Initially, as before, we train the main network using five distinct *heads*, each responsible for values of a within the interval $[0.0, 1.5]$. We conduct this training over 3×10^6 epochs for two separate main networks. In one of this set of networks, we apply UR as an extra loss term. The derived solutions, along with the determinant of the metrics for both networks, are displayed in Figure 6. Subsequently, the main networks are fixed, and a new *head* is trained over 7×10^6 epochs to facilitate TL to $a = 1.75$. The TL results for both networks, along with their relative error—which is calculated using equation (11)—are illustrated in Figure 7.

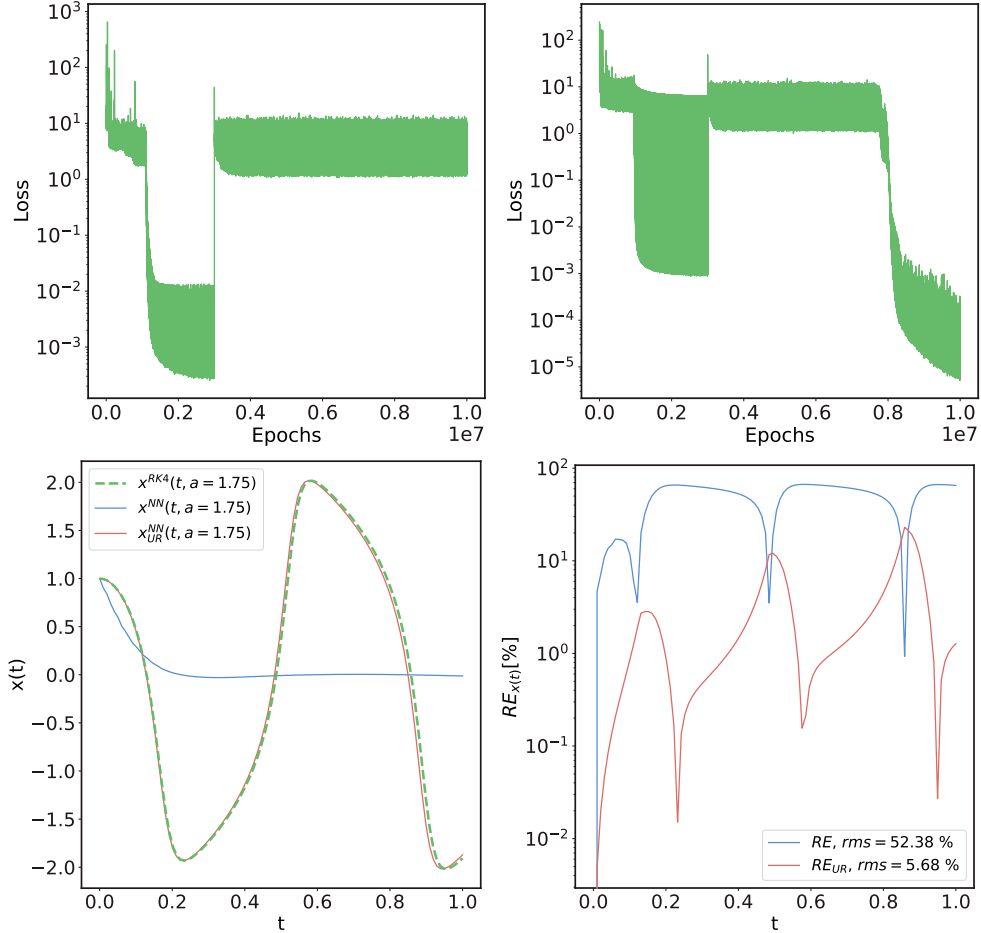


Fig. 7 TL of van der Pol oscillator for $a = 1.75$. **Top**: Loss functions for the TL without UR (left) and with UR (right) on the MH *bodies*. TL starts at epoch $3 \cdot 10^6$. **Bottom left**: Solution for $x^{NN}(t)$ for cases without UR (solid blue), with UR (solid red) compared to the RK4-numerical solution (dashed green). **Bottom right**: Relative error (in %) for cases with UR (red) and without UR (blue). In the legend, we show the value of the root mean square (rms) for each case.

This paragraph outlines the key aspects of both the architecture and the training methodology. In constructing the MH *body*, we employed two fully connected neural networks (FCNN), each having two input units and an output size of 128, with four layers consisting of 64 neurons each. The **Tanh** function was selected as the activation function for both networks. For the *heads*, we selected an FCNN with 128 input units, a single output dimension, and two layers, each containing 64 neurons. The training of the body involved the **adam** optimizer, initialized with a learning rate of 10^{-3} . A learning rate scheduler was applied to decrease it by 2.5% every 15,000 epochs. For TL, we also used the **adam** optimizer, starting with an initial learning rate of 10^{-3} , and a scheduler decreasing it by 4% every 70,000 epochs. The training dataset consisted of

100 evenly distributed points in t ranging from 0 to 1. To prevent overfitting, random noise was added to these points at each epoch. A UR penalty, with $\lambda = 4 \cdot 10^{-5}$, was applied every 100 epochs as an additional loss.

3.3 Einstein Field Equations in AdS background

Before going into details of this case, it is important to note that the level of difficulty here is significantly higher than in the previous examples. The ODEs considered earlier served mainly as toy models to illustrate both the MH setup and UR technique, and their solutions and behaviors are well understood. However, the example presented in this section has only been solved for not very stiff regimes [22].

Moreover, its resolution involves solving a system of seven ordinary highly non-linear ODEs for approximately 70 BCs, and recovering a free-form function appearing within the equations that is uniquely determined by these BCs. Consequently, this stands out as one of the most challenging setups for testing the algorithms introduced thus far.

As previously indicated, our system comprises seven first-order, non-linear ODEs (14a)–(14g), with six being linearly independent. At first glance, one can observe that the first three equations are simply redefinitions of the derivatives of the variables $\tilde{\Sigma}$, \tilde{A} y ϕ . This arises because the Einstein Field Equations (EFE) are second-order differential equations, which have been rewritten as first-order equations. For a detailed discussion on the physical motivation behind these redefinitions, the reader is referred to [22] and references therein.

$$\nu_{\Sigma} - \tilde{\Sigma}' = 0, \quad (14a)$$

$$\nu_A - \tilde{A}' = 0, \quad (14b)$$

$$\nu_{\phi} - \phi' = 0, \quad (14c)$$

$$\nu'_{\Sigma} + \frac{2}{3}\tilde{\Sigma}\nu_{\phi}^2 = 0, \quad (14d)$$

$$u^2 \tilde{\Sigma} \nu'_A + \frac{8}{3} V(\phi) \tilde{\Sigma} + \nu_A \left(3u^2 \nu_{\Sigma} - 5u \tilde{\Sigma} \right) + \tilde{A} \left(8\tilde{\Sigma} - 6u \nu_{\Sigma} \right) = 0, \quad (14e)$$

$$u^2 \tilde{\Sigma} \tilde{A} \nu'_{\phi} - \tilde{\Sigma} \frac{dV}{d\phi} + \nu_{\phi} \left(-3u \tilde{A} \tilde{\Sigma} + u^2 \tilde{\Sigma} \nu_A + 3u^2 \nu_{\Sigma} \tilde{A} \right) = 0, \quad (14f)$$

$$\left(u \nu_{\Sigma} - \tilde{\Sigma} \right) \left(u^2 \tilde{\Sigma} \nu_A + 2u^2 \tilde{A} \nu_{\Sigma} - 4u \tilde{A} \tilde{\Sigma} \right) - \frac{2}{3} u \tilde{\Sigma}^2 \left(u^2 \tilde{A} \nu_{\phi}^2 - 2V(\phi) \right) = 0. \quad (14g)$$

The independent variable is u . The six functions (dependent variables) are $\vec{\psi}(u) \equiv \left(\tilde{\Sigma}(u), \tilde{A}(u), \phi(u), \nu_{\Sigma}(u), \nu_A(u), \nu_{\phi}(u) \right)$. Looking at Eqs. (14e)–(14g), we can see a free function $V(\phi)$ and its derivative. Evidently, for different $V(\phi)$, one would get different equations, and thus different solutions $\vec{\psi}(u)$.

The BCs are given by:

$$\tilde{\Sigma}|_{u=0} = 1 , \quad (15a)$$

$$\tilde{A}|_{u=0} = 1 , \quad (15b)$$

$$\phi|_{u=0} = 0 , \quad (15c)$$

$$\nu_\phi|_{u=0} = 1 , \quad (15d)$$

$$\tilde{\Sigma}_{u=1} = (S/\pi)^{1/3} , \quad (15e)$$

$$\tilde{A}|_{u=1} = 0 , \quad (15f)$$

$$\nu_A|_{u=1} = -4\pi T . \quad (15g)$$

The BC for $\tilde{\Sigma}(u)$ and $\nu_A(u)$ at $u = 1$ depends on a pair of values $\{T, S\}$ (temperature and entropy). It should be noted that there is an additional boundary condition present. Since we are not solving the equations exactly, giving additional constraints (when available) is helpful for the learning process.

The physical reasoning associated with this system primarily clarifies two aspects. Firstly, there will be a specific relation between temperature and entropy $S = S(T)$, meaning that for a choice of T , the value of S is fixed. Secondly, there is an exact one to one correspondence between the free function $V(\phi)$ and the relation $S(T)$.

In this setting, we define the *direct problem* as follows:

1. **Select a specific $V(\phi)$.** ⁷ A chosen $V(\phi)$ specifies an entire family of ODEs, with different BCs giving rise to variations within that family.
2. **Choose N distinct sets of boundary conditions, $\{\text{BC}_i\}_{i=1}^N$.**
3. **Numerically solve the ODE systems** defined by Eqs. (14a)–(14g) together with each of the BC_i , using standard methods (e.g., `NDSolve` in *Mathematica*, see [30, 31]). Denote the corresponding solutions by $\{\vec{\psi}_i(u)\}_{i=1}^N$.
4. **Evaluate each solution $\tilde{\Sigma}_i(u)$ and $\nu_{A,i}(u)$ at $u = 1$ to obtain S_i and T_i via Eqs. (15e) and (15g), respectively.** By pairing each T_i with its corresponding S_i , one obtains the $S(T)$ curve associated with the initial choice of $V(\phi)$

Note again that the direct problem can be handled with traditional numerical methods.

Let us now discuss the **inverse problem**: we take a sample of N points from a chosen $S(T)$ relation, which specifies a bundle $\{\text{BC}_i\}_{i=1}^N$. Consequently, the “full solution” $\{\vec{\psi}_i(u)\}_{i=1}^N$ becomes a set of N different solutions to Eqs. (14a)–(14g) that must be found. Even though we know there is a corresponding function $V(\phi)$ related to the chosen $S(T)$ /BCs, we do not actually know this function; it remains a free function determined by the solutions $\phi_i(u) \in \vec{\psi}_i(u)$ for each $i = 1, \dots, N$.

⁷The function $V(\phi)$ must satisfy certain constraints on its value and derivatives near $\phi = 0$ to ensure the resulting equations are well-defined. For a detailed discussion, see [22, 30].

The task is **finding the unique free function** $V(\phi)$ such that the corresponding ODE family admits solutions $\{\vec{\psi}_i(u)\}_{i=1}^N$ **for all** $\{T_i, S_i\}$ **in the bundle**, while simultaneously determining those solutions. Although each $\{T_i, S_i\}$ (and thus each set of boundary conditions) leads to a different solution $\vec{\psi}_i(u)$, all solutions must share the same free function $V(\phi)$.

Solving this inverse problem with traditional methods is not possible, because the equations must be fully specified before numerical integration can proceed—they cannot depend on $V(\phi)$ when it is treated as a free function.

In [22], we and our collaborators developed an algorithm that uses PINNs to solve this problem. To check that the algorithm worked, we followed the work by [30], where a theoretical potential $V^{\text{th}}(\phi)$ is chosen, and the direct problem is solved numerically to obtain $S^{\text{th}}(T)$. Then, we solved the inverse problem, giving this $S^{\text{th}}(T)$ as input to our PINNs setup as BCs. We find the solutions and recover the free function, $V^{\text{PINN}}(\phi)$. In this way, we are able to compare the original and recovered free functions $V^{\text{th}}(\phi)$ and $V^{\text{PINN}}(\phi)$, respectively. Also, by solving numerically once more the direct problem using now the recovered $V^{\text{PINN}}(\phi)$, we obtained the associated $S^{\text{PINN}}(T)$, which can again be compared with the original $S^{\text{th}}(T)$.

However, besides being a challenging problem due to its inverse nature, there are several other complications. The primary complication arises from the morphology of $S(T)$, which can induce features in the associated $V(\phi)$ at vastly different scales. This separation of scales significantly increases the stiffness of the problem. *In general, when a system exhibits features across multiple scales, numerical methods must accommodate the rapid variations alongside the slower ones, leading to stiffness.* In our case, we quantify the complexity of the morphologies of $S(T)$, and thus indirectly the stiffness of the problem, using a single parameter ϕ_M . Specifically, we operate within the model selected in [30], where the parameter ϕ_M is integral to the choice of $V(\phi; \phi_M)$ when solving the direct problem. Lower values of ϕ_M correspond to richer morphologies of the associated $S(T)$, introducing more pronounced scale separations.

Subsequently, we tackle the inverse problem using selections of $S(T)$ with known morphological relationships to ϕ_M . While a general choice of $S(T)$ might not be governed by a single parameter, within the same physical context, the correspondence between $S(T)$ and $V(\phi)$ remains intact. It is important to note that the link between scale separation and stiffness, while observed and utilized in our framework, is not derived from a formal mathematical proof but rather from empirical and heuristic understanding. Therefore, even though the stiffness of our Einstein Field Equations (EFE) problem is influenced by the morphology of $S(T)$, we refer to ϕ_M as a “stiffness parameter” analogous to the parameter δ in the flame equation (10) and the parameter a in the Van der Pol (VdP) equation (12). Lower values of ϕ_M exacerbate the problem’s stiffness, making it increasingly difficult to recover the free function. This difficulty persists until the original PINN setup either fails to recover $V(\phi)$ within an acceptable error margin or, in cases of extreme stiffness, fails to recover it altogether, including its most fundamental features, such as the position ϕ_H and scale $V(\phi_H)$ of the critical points. For a more in-depth discussion on the stiffness of the problem, the features in $V(\phi)$, and the morphologies of $S(T)$, we refer the reader to our previous work [22], particularly Figures 1, 2, and 13.

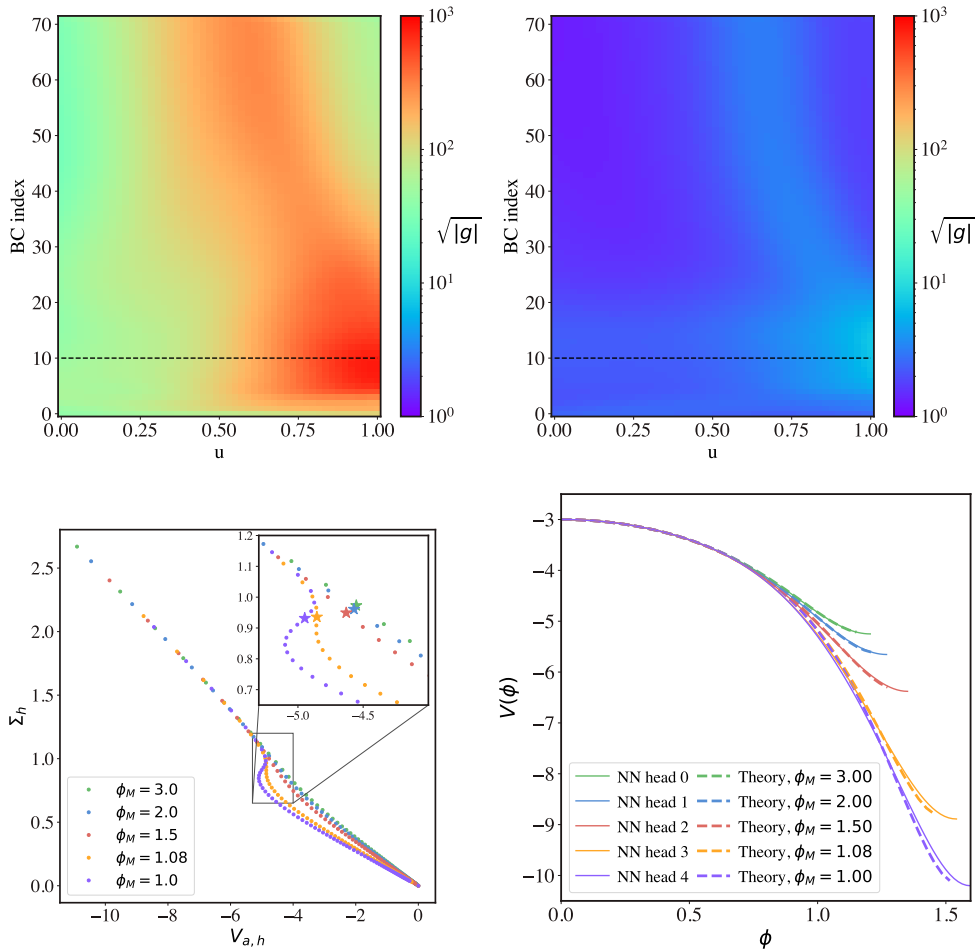


Fig. 8 Training of the MH body for the EFE. **Top:** Metric determinant for cases without UR (left) and with UR (right), for the head corresponding to the parameter $\phi_M = 1$, for one of the solution functions, $\nu_\Sigma(u) \in \vec{\psi}(u)$. In both panels, the black, dashed, horizontal line corresponds to the ODE problem given by the BC that is marked with a purple star in the bottom, left panel (theory with $\phi_M = 1$). **Bottom left:** Different input points given to the body that come from different choices of $S(T)_{\phi_M}$. Marked with a star, we show the BC point with index $i = 10$ for all ϕ_M . This point approximately tracks where the equations become stiffer within the corresponding ϕ_M family. **Bottom right:** The recovered $V^{\text{NN}}(\phi; \phi_M)$ coming from the MH *body* are shown in solid lines, while the theoretical $V^{\text{th}}(\phi; \phi_M)$ are shown in dashed lines.

In this context, we introduce a **multi-head (MH) approach**: we supply our MH PINN framework with five increasingly stiff curves $S(T)_{\phi_M}$, corresponding to $\phi_M = \{3.0, 2.0, 1.5, 1.08, 1.0\}$ (see Fig. 8, bottom panels). Through its shared *body*, the MH PINN learns the latent space of solutions and free functions associated with the various morphologies of $S(T)_{\phi_M}$. Subsequently, each *head* projects down from this shared latent space to produce a specific $V^{\text{PINN}}(\phi; \phi_M)$, as well as the corresponding ODE solutions $\vec{\psi}_{i, \phi_M}$, for the BCs specified by each $\{T_i, S_i\}_{\phi_M}$.

As explained in Sec. 2.2 and 2.3, we then use the frozen latent space to perform TL to stiffer regimes. In our approach, we do so for two new $S(T)$ curves corresponding to $\phi_M = 0.9$ and $\phi_M = 0.7$. We test UR on both cases and display our findings in figures 8 (training of the *body*), 9 (case with $\phi_M = 0.9$) and 10 (case with $\phi_M = 0.7$).

Observe that in this configuration, the UR possesses an extra dimension, making it three-dimensional. The first dimension is due to the independent variable u , the second dimension is associated with the i -index, which labels each BC along the path $S(T) \rightarrow \{T_i, S_i\}$, and the third dimension is linked with the *stiffness parameter* ϕ_M , which parametrizes the various morphologies of $S(T)$. The top panels of Fig. 8 illustrate a slice of $\sqrt{|g|}$ perpendicular to the ϕ_M direction, representing a particular $S(T)_{\phi_M}$ or $V(\phi; \phi_M)$.

Before we present the results, we summarize the architecture and training procedure for the EFE case. These procedures are identical in scenarios both with and without UR to ensure a fair comparison of their performance. Each solution function in $\vec{\psi}(u) = (\tilde{\Sigma}(u), \tilde{A}(u), \phi(u), \nu_{\Sigma}(u), \nu_A(u), \nu_{\phi}(u))$ is produced by an individual FCNN. The architecture of these NNs consists of [32, 32, 32, 32, 128] layers for the main *bodies* and [16, 16] for the five *heads*, all utilizing **Tanh** activation. The free function $V^{\text{PINN}}(\phi)$ is derived from another FCNN with a *body* structured as [32, 32, 32, 128] and five *heads* composed of [64, 64], with **SiLU** as the activation for both the *body* and *heads*. The optimizer used for *body* training and transfer learning is **adam**, starting with an initial learning rate of $1 \cdot 10^{-3}$. As part of the scheduling process, the learning rate is reduced by 1.5% every 5000 epochs, both in training the *body* and in transfer learning. In scenarios with UR, it is imposed in the loss calculation every 500 iterations, with a global coefficient $\lambda = 5 \cdot 10^{-8}$.

TL under UR exhibited significant improvement in recovering the free function $V(\phi; \phi_M)$ and the associated $S(T)_{\phi_M}$. Specifically, for TL to $\phi_M = 0.9$, our UR approach accomplished a twofold improvement in the recovery of $V(\phi, 0.9)$, reducing root mean square (rms) from roughly 5% to about 3%. Consequently, this also signified a twofold improvement in $S(T)_{0.9}$, with rms decreasing from around 13% to about 6%. In the context of $\phi_M = 0.7$, results are less precise overall due to significant increases in problem stiffness. Nevertheless, there is a threefold enhancement through UR in retrieving $V(\phi, 0.7)$, with rms dropping from approximately 64% to approximately 22%, and a sevenfold improvement in $S(T)_{0.7}$, reducing rms from around 178% to roughly 26%. In both scenarios, UR demonstrates improvements in recovery, and for $\phi_M = 0.7$, it enables a closer TL approximation, whereas the conventional MH case resulted in extraordinarily large errors.

4 Conclusions

We have presented new techniques to solve nonlinear, multiscale differential equations (DEs) with Physics-Informed Neural Networks (PINNs), placing special emphasis on inverse problems. These techniques, which we term multi-head (MH) and Unimodular Regularization (UR), have proved effective in various examples of nonlinear, multiscale DEs. We have shown that, by using a single NN structure (the *body*) shared across

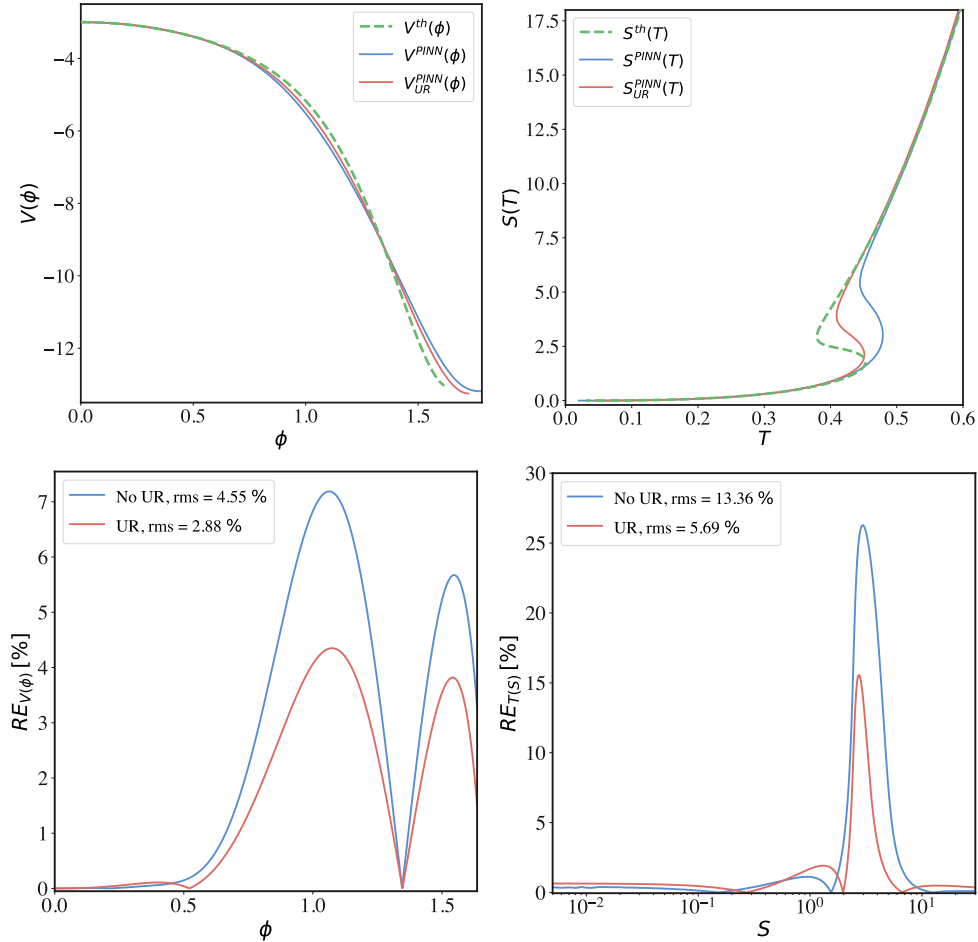


Fig. 9 TL of EFE for $\phi_M = 0.9$. **Top left:** Recovered functions $V^{\text{PINN}}(\phi)$ through TL without UR (solid blue), and with UR (solid red), compared with the theoretical function (dashed green). **Top right:** $S^{\text{PINN}}(T)$ relations associated to the recovered $V^{\text{PINN}}(\phi)$ without and with UR, compared to the theoretical one (which is also the initial input in the TL procedure). **Bottom:** Relative errors for both the recovered $V^{\text{PINN}}(\phi)$ (left) and associated $S^{\text{PINN}}(T)$ (right) for the cases without UR (blue) and with UR (red). In the legend, we show the value of the root mean square (rms) for each case.

multiple NN substructures (*heads*), MH training can learn the broader space of solutions for variations of the DE. We verified this approach using variations in the DEs' parametric dependence, initial conditions (ICs), and boundary conditions (BCs). The learned general solution space (or latent space) can then be leveraged to find specific solutions for new DE variations under more extreme or stiffer regimes, even if the MH *body* was not initially trained for these cases. This approach is known as transfer learning (TL). Furthermore, we have developed UR, a technique that imposes specific conditions on the determinant of the metric tensor induced by embedding the latent space into the input/parameter space. This idea is grounded in differential geometry

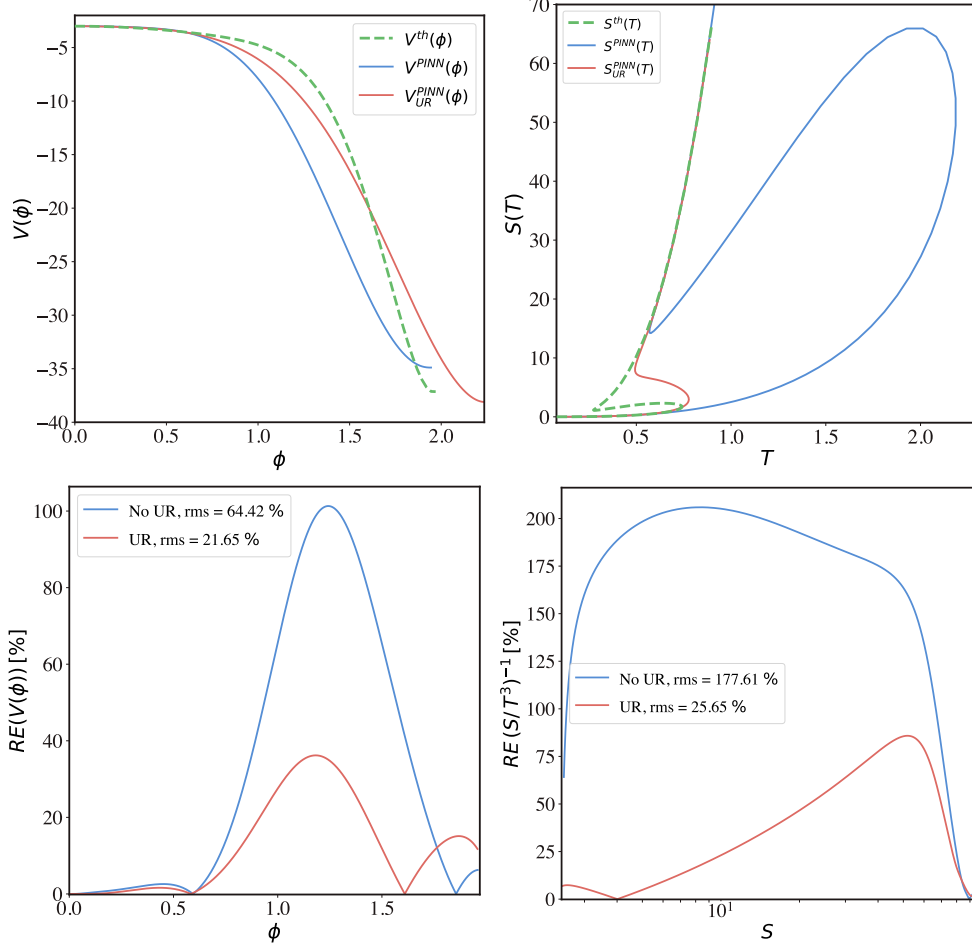


Fig. 10 TL of EFE for $\phi_M = 0.9$. **Top left:** Recovered functions $V^{\text{PINN}}(\phi)$ through TL without UR (solid blue), and with UR (solid red), compared with the theoretical function (dashed green). **Top right:** $S^{\text{PINN}}(T)$ relations associated to the recovered $V^{\text{PINN}}(\phi)$ without and with UR, compared to the theoretical one. **Bottom:** Relative errors for both the recovered $V^{\text{PINN}}(\phi)$ (left) and associated $S^{\text{PINN}}(T)$ (right) for the cases without UR (blue) and with UR (red). In the legend, we show the value of the root mean square (rms) for each case.

and draw inspiration from General Relativity. The imposed conditions quantify and regulate the latent space's sensitivity to specific variations in the DEs. We have found that combining the MH approach with UR in the latent space of solutions significantly enhances PINN efficiency, facilitating the TL process and thus enabling more effective solution discovery.

Our results are derived by implementing the MH technique both with and without UR, then comparing the solutions obtained to a numerical baseline. We apply this approach to three distinct sets of ordinary differential equations (ODEs): the

flame equation, the van der Pol (damped) oscillator, and the Einstein Field Equations (EFEs).

For the flame equation, a nonlinear first-order ODE, UR reduces the root mean square error (rms) from 35.1% to 0.5%. For the van der Pol oscillator, a nonlinear second-order ODE, UR enables transfer learning to highly stiff regimes, resulting in a root mean square error (rms) of 5.7%. Finally, for the Einstein Field Equations (EFE)—an inverse, nonlinear system of first-order ODEs—we can simultaneously recover an approximate free-form function that appears in the DEs, together with the corresponding solutions. The free function is inferred from its physically motivated correspondence to a physical relation between different BCs (an implicit mapping in the equations). In this final case, we applied transfer learning to two increasingly stiff regimes. The first transfer showed a factor-of-2 improvement with UR. The second demonstrated a factor-of-3 improvement—or factor-of-7 when comparing the recovered free-form function or the corresponding BC relation. In this second instance, only approximate recovery of the full solution’s morphology is achieved when UR is included.

We have provided three examples demonstrating that, with these algorithms, it is possible to tackle very complex problems in various scientific fields where unknown phenomena must be discovered through the inversion of differential equations, as shown in the last provided example. Consequently, these algorithms could be extremely powerful, as such problems arise in a wide range of areas, including General Relativity, complex fluid dynamics, social sciences, and beyond.

Acknowledgements

PT is supported by the project “Dark Energy and the Origin of the Universe” (PRE2022-102220), funded by MCIN/AEI/10.13039/501100011033. Funding for the work of PT, PT and RJ was partially provided by project PID2022-141125NB-I00, and the “Center of Excellence Maria de Maeztu 2020-2023” award to the ICCUB (CEX2019- 000918-M) funded by MCIN/AEI/10.13039/501100011033.

References

- [1] Pinney, E.: Nonlinear differential equations. Bulletin of the American Mathematical Society (1955)
- [2] Mathematical problems in engineering: Special issue on nonlinear differential equations and their applications. Mathematical Problems in Engineering (2025)
- [3] Zou, Z., Karniadakis, G.: L-hydra: Multi-head physics-informed neural networks (2023)
- [4] Desai, S., Mattheakis, M., Joy, H., Protopapas, P., Roberts, S.: One-Shot Transfer Learning of Physics-Informed Neural Networks (2022)

- [5] Zhou, W., et al.: Data-guided physics-informed neural networks for solving inverse problems in partial differential equations. arXiv preprint arXiv:2407.10836 (2024)
- [6] Berardi, M., et al.: Inverse physics-informed neural networks for transport models in porous materials. arXiv preprint arXiv:2407.10654 (2024)
- [7] Lei, W., Protopapas, P., Parikh, J.: One-Shot Transfer Learning for Nonlinear ODEs. arXiv e-prints, 2311–14931 (2023) <https://doi.org/10.48550/arXiv.2311.14931> arXiv:2311.14931 [cs.LG]
- [8] Pellegrin, R., Bullwinkel, B., Mattheakis, M., Protopapas, P.: Transfer learning with physics-informed neural networks for efficient simulation of branched flows. CoRR **abs/2211.00214** (2022)
- [9] Baldan, M., Di Barba, P., Lowther, D.A.: Physics-informed neural networks for inverse electromagnetic problems. IEEE Transactions on Magnetics **59**(2), 1–5 (2023)
- [10] Kaul, P., Lall, B.: Riemannian curvature of deep neural networks. IEEE Transactions on Neural Networks and Learning Systems **31**(4), 1410–1416 (2020) <https://doi.org/10.1109/TNNLS.2019.2919705>
- [11] Chen, J., Huang, T., Chen, W., Liu, Y.: Thoughts on the Consistency between Ricci Flow and Neural Network Behavior. arXiv e-prints, 2111–08410 (2021) <https://doi.org/10.48550/arXiv.2111.08410> arXiv:2111.08410 [cs.LG]
- [12] Glass, S., Spasov, S.E., Lio', P.: Riccinets: Curvature-guided pruning of high-performance neural networks using ricci flow. ArXiv **abs/2007.04216** (2020)
- [13] Sun, L., Huang, Z., Wu, H., Ye, J., Peng, H., Yu, Z., Yu, P.: Deepricci: Self-supervised graph structure-feature co-refinement for alleviating over-squashing, pp. 558–567 (2023). <https://doi.org/10.1109/ICDM58522.2023.00065>
- [14] Coddington, E.A., Levinson, N.: Theory of Ordinary Differential Equations. Tata McGraw-Hill Education, ??? (1955)
- [15] Flamant, C., Protopapas, P., Hunter, D.: Solving differential equations using neural network solution bundles. arXiv preprint arXiv:2006.14372 (2020)
- [16] Chen, F., Sondak, D., Protopapas, P., Mattheakis, M., Liu, S., Agarwal, D., Giovanni, M.D.: Neurodiffeq: A python package for solving differential equations with neural networks. Journal of Open Source Software **5**(46), 1931 (2020) <https://doi.org/10.21105/joss.01931>
- [17] Lu, L., Meng, X., Mao, Z., Karniadakis, G.E.: Deepxde: A deep learning library for solving differential equations. SIAM Review **63**(1), 208–228 (2021)
- [18] Karniadakis, G.E., Kevrekidis, I.G., Lu, L., Perdikaris, P., Wang, S., Yang, L.:

- Physics-informed machine learning. *Nature Reviews Physics* **3**(6), 422–440 (2021)
- [19] Hairer, E., Wanner, G.: *Solving Ordinary Differential Equations II: Stiff and Differential-algebraic Problems*. Springer Series in Computational Mathematics, vol. 14. Springer, ??? (1996)
- [20] Lambert, J.D.: *Numerical Methods for Ordinary Differential Systems: the Initial Value Problem*. John Wiley & Sons, Inc., ??? (1991)
- [21] Raissi, M., Perdikaris, P., Karniadakis, G.E.: Physics-informed neural networks: A deep learning framework for solving forward and inverse problems involving nonlinear partial differential equations. *Journal of Computational Physics* **378**, 686–707 (2019)
- [22] Bea, Y., Jimenez, R., Mateos, D., Liu, S., Protopapas, P., Tarancón-Álvarez, P., Tejerina-Pérez, P.: Gravitational duals from equations of state. *JHEP* **07**, 087 (2024) [https://doi.org/10.1007/JHEP07\(2024\)087](https://doi.org/10.1007/JHEP07(2024)087) [arXiv:2403.14763](https://arxiv.org/abs/2403.14763) [hep-th]
- [23] Dissanayake, M., Phan-Thien, N.: Neural-network-based approximations for solving partial differential equations. *communications in Numerical Methods in Engineering* **10**(3), 195–201 (1994)
- [24] Lagaris, I.E., Likas, A.C., Papageorgiou, D.G.: Neural-network methods for boundary value problems with irregular boundaries. *IEEE Transactions on Neural Networks* **11**(5), 1041–1049 (2000) <https://doi.org/10.1109/72.870037> . Conference Name: IEEE Transactions on Neural Networks
- [25] Mattheakis, M., Propson, T., Guo, P., Kaxiras, E.: *Hamiltonian Neural Networks for Solving Equations of Motion* (2021)
- [26] Sirignano, J., Spiliopoulos, K.: Dgm: A deep learning algorithm for solving partial differential equations. *Journal of Computational Physics* **375**, 1339–1364 (2018) <https://doi.org/10.1016/j.jcp.2018.08.029>
- [27] Zhu, Y., Zabaras, N., Lu, L., Perdikaris, P.: Physics-constrained deep learning for high-dimensional surrogate modeling and uncertainty quantification without labeled data. *Journal of Computational Physics* **394**, 56–81 (2019) <https://doi.org/10.1016/j.jcp.2019.05.048>
- [28] Alvarez, E., Velasco-Aja, E.: *A Primer on Unimodular Gravity*, (2023). https://doi.org/10.1007/978-981-19-3079-9_15-1
- [29] Carballo-Rubio, R., Garay, L.J., García-Moreno, G.: Unimodular gravity vs general relativity: a status report. *Class. Quant. Grav.* **39**(24), 243001 (2022) <https://doi.org/10.1088/1361-6382/aca386> [arXiv:2207.08499](https://arxiv.org/abs/2207.08499) [gr-qc]
- [30] Bea, Y., Mateos, D.: Heating up Exotic RG Flows with Holography. *JHEP* **08**,

034 (2018) [https://doi.org/10.1007/JHEP08\(2018\)034](https://doi.org/10.1007/JHEP08(2018)034) [arXiv:1805.01806](https://arxiv.org/abs/1805.01806) [hep-th]

- [31] Gubser, S.S., Nellore, A.: Mimicking the QCD equation of state with a dual black hole. *Phys. Rev. D* **78**, 086007 (2008) <https://doi.org/10.1103/PhysRevD.78.086007> [arXiv:0804.0434](https://arxiv.org/abs/0804.0434) [hep-th]